An enhanced computational modelling of rock fracture-induced seismicity: the discrete element method (DEM) approach

Kenneth Imo-Imo Eshiet, kenneth.eshiet@see-ed.com, kenieshiet@yahoo.com
Sustainable Energy Environmental and Educational Development (SEEED) Ltd, USA

Yong Sheng, y.sheng2@wlv.ac.uk
University of Wolverhampton, UK

Dongmin Yang, d.yang@leeds.ac.uk
University of Leeds, UK

Rizgar Rassul Maolod, cnrrm@leeds.ac.uk
University of Leeds, UK

Abstract
An advancement of the discrete element method (DEM) is presented that improves simulation of seismicity in rock materials. The developed model builds on previous DEM procedures for imitating acoustic emissions and micro-seismicity in rocks. Currently, formulations that govern DEM techniques identify the breakage of inter-particle bonds and creation of cracks as a singular source of micro-seismic event. They implement a fixed criterion for clustering which fails to adequately account for the involvement of nearby particles and contacts, and does not systematically categorise the spatial, temporal and intensity characteristics of acoustic emissions and micro-seismic events. The revised DEM introduces a concept that fully recognises contributions from particles around source cracks, while integrating the motion and forces on neighbouring particles and contacts. This concept also involves the adoption of a changeable combination factor for establishing, distinguishing and recording acoustic emission/micro-seismic events. This new approach is validated against two physical laboratory experiments on Springwell sandstone and Inada granite: uniaxial and triaxial compression, and fluid injection. The distribution of acoustic emission events from the numerical model matches those visualise in physical experiments. The b_values, sizes of crack aperture and patterns of source mechanisms are also in good agreement with experimental results and, in some instances, field-scale natural conditions.

Keywords: Discrete element method, seismicity, acoustic emission, fracture, subsurface, fluid injection

1 Introduction

Seismicity is an accepted measure/phenomenon that describes the frequency, intensity, magnitude and distribution of earthquake activities or earth tremors within a given area. An excellent way of assessing the seismicity within a given body is to monitor and record associated acoustic emissions (AE). Acoustic emissions is the process of transient radiation of acoustic, elastic waves within a solid mass when it is subjected to internal irreversible alterations. Acoustic waves are emitted due to the rapid discharge of localised stress energy. The mechanisms and principles of acoustic emissions are widely applied in the study of underground structures and, to a large extent, have proven to be sufficient in enhancing understanding as well as predictions of seismic events in the subsurface (Pettitt and King, 2007). The onset and propagation of fractures, plastic deformation, external loading and temperature gradients are known irreversible damage mechanisms or sources of irreversible damage that cause seismic events, as indicated through the release of acoustic waves across rock formations. Hence, over time and in tandem with ultrasonic velocities and

recordings of petrophysical properties, the concept of acoustic emissions has been developed into a veritable tool for investigating phenomena, and the behaviour of natural and engineered structures where there are mechanical, hydraulic and thermal alterations in the environment (Pettitt and King, 2007, Young and Pettitt, 2000). In many cases seismicity is generated due to natural causes; however, the number and frequency of induced seismic events related to anthropogenic activities, that are significant in nature, have risen considerably (Foulgar *et al*., 2018). Some culpable human actions are extraction of hydrocarbons, groundwater, geothermal fluids and minerals; quarrying, construction of high rising structures, impoundment of watercourses to restrain natural flow, etc. (Foulgar *et al*., 2018).

With proper acoustic emission analysis and interpretation, it is possible to study failure processes in rocks and other engineered materials (Aker *et al*. 2014, Michlmayr, *et al.,* 2012) and to characterise fracturing processes in terms of origin, direction of growth, density and type (Graham *et al.,* 2010, Pettitt and King, 2007). As demonstrated by Lockner *et al.* (1991), inversion of acoustic emission arrival-time data can be used to locate their corresponding hypocentres, this is valuable information required to depict fracture proliferation. At the field scale, this concept is used to identify origins of earthquakes or subsurface explosions. By extension, acoustic emission is a useful tool for studying fracturing caused by specific conditions such as changes in pore pressure, polyaxial stresses, fluid injection, and other processes including well breakouts and the creation of compaction bands (Aker *et al*., 2014).

The application of acoustic emission and other parameters related to microseismicity in studies of subsurface geomechanics has become increasingly versatile and widely reported. Recordings of acoustic emission rates has been applied by Aker *et al*. (2014) to delineate the various stages of macroscopic deformation and failure of rocks, illustrating how these relate to the corresponding stress-strain evolution. Aker *et al*. (2014) also investigated the impact of rock damage and stresses on ultrasonic acoustic waves (P and S-wave velocities). In Filipissi, *et al.* (2015), trends of acoustic emission (AE) parameters including wave amplitude, duration, energy and root mean square (RMS) of acoustic emission signals, in relation to the load-time sequence during uniaxial compression tests on andesite rocks, were used to determine damage evolution and to predict fracturing processes. Changes in microseismic events observed by Maghsoudi *et al.* (2018) during field hydraulic fracturing operations provided evidence of aggravations that could contribute to the trigger of earthquakes. The patterns of microseismic events rendered further insights on changes in stress, fault strength, onset of rupture and fracture propagation. Numerical simulations incorporating models for microseismic frequency-magnitude distributions (e.g., Wangen, 2018) have also been applied to predict damage and hydraulic fracturing of rocks. Many of these models attempt to capture mechanisms of microseismicity triggered by fluid injection and flow (e.g., Wangen, 2018, Lei *et al*., 2016, Rothert and Shapiro, 2003).

There are several approaches for simulating seismic activities that are associated with deformation, fracturing and failure of materials. Models developed are based on continuum methods, discontinuum methods or hybrids of the two techniques. A summarised cross-section of these methodologies as applied in studies of seismicity is discussed, for instance, in Lisjak *et al.* (2013). Continuum methods are built on the assumption that the body is a single continuous computational domain with mechanics formulations governed by plasticity and damage theories (Lisjak and Grasselli, 2014). In continuum damage models, acoustic emission is generally linked to individual damaged elements and dissipation of the associated elastic strain energy is related to the seismic energy discharged (Zhu *et al*., 2010, Tang and Kaisar, 1998, Tang, 1997). A few continuum-based damage models are shown to be capable of depicting the power-law distribution between the magnitude and population of damage events.

Discontinuum methods are alternatives ways of simulating seismic events and their effects. These are formulated in a variety of forms including lattice models (e.g., Hu and Jia, 2016; O'Brien and Bean, 2011), particle-based models (e.g., Yoon *et al.,* 2017; Yoon *et al.,* 2015; Zang *et al*. 2013; Wang, 2008; Al-Busaidi *et al.,* 2005; Hazzard and Young, 2004; Hazzard and Young, 2002) and hybrid models (e.g., Mohammadipour and Willam, 2016; Zhao, *et al*., 2014; Lisjak *et al.,* 2013). Discrete element method (DEM) is one of such particle-based numerical modelling techniques where the material domain is represented by an assembly of particles bonded together at contact points. With this approach, seismic events are triggered when inter-particle bonds are broken due to the overwhelming impact of stresses. Seismicity is manifested via the release of stored strain energy in the form of kinetic energy. Ways by which seismic source information are calculated for acoustic emission and microseismicity are presented in Hazzard and Young (2000, 2002, and 2004). In this study, the capability of Hazzard and Young's computational techniques is advanced by 1) expanding the recordings of acoustic emission/microseimicity to include contributions from forces applied on particles around the source crack, 2) allowing for a flexible rupture speed as a substitute to maintaining fixed values, and 3) adopting a changeable combination factor with respect to seismic sources. The combination factor controls the grouping of events into distinctive clusters.

2 **Theoretical background on seismicity**

Earthquakes and seismic activities in general are best understood and predicted by monitoring and interpreting acoustic emissions and microseismic events. The difference between acoustic emissions and microseismic events lie in the level and range of wave frequency. Acoustic emission is the radiation of small high-frequency elastic acoustic waves above 35 kHz, whereas, a microseismic event is characterised by larger low-frequency acoustic waves (0.5-10 kHz) (Cheon, *et al.,* 2008; Hazzard and Young, 2004; Young and Baker, 2001). This simply implies that the frequency of microseismic event signals are lower than those of acoustic emission. The calculations, observations and interpretations described herein is applicable in the same manner to both types of seismic motion frequencies.

2.1 **The frequency and magnitude of seismic activities**

2.1.1 **Establishing the frequency-magnitude relationship**

The well-known *Gutenberg and Richter* relationship linking the magnitude to the number of earthquakes above a given intensity/amplitude (Gutenberg and Richter, 1956) is a power law relation that can be directly applied in the study of acoustic emissions in rocks by relating the frequency (number) of events to their corresponding magnitude (Lei and Ma, 2014; Lisjak *et al.,* 2013; Ji and Di, 2013; Hazzard and Young, 2004). The distribution of acoustic emission can therefore be specified in terms of a power law relationship (Lisjak, *et al*., 2013):

$$N(> A_p) = a(A_p)^{-b} \qquad [1]$$

Where N is the number of acoustic emission events which have amplitudes that exceed A_p, A_p is the maximum amplitude of acoustic emission and the constant parameters are a and b. Equation 1 can be made linear by conversion to logarithmic coordinates, expressed as

$$\log_{10} N = a - b \log_{10} A_p \qquad [2a]$$

Alternatively, $\log_{10} A_p$ in Equation 2a may be denoted as the magnitude of acoustic emission given by a single parameter, M. N will therefore be the number of acoustic emission events with magnitude equal or above M. Equation 2a becomes (Lisjak *et al.,* 2013; Ji and Di, 2013; Scholz, 1968):

$$\log_{10} N = a - bM \quad [2b]$$

2.1.2 **Magnitude of seismic events**

The seismic moment (M_o) is a measure of earthquake size and defined by Aki (1966, 1967) as

$$M_o = G\Delta dA \quad [3]$$

Where, G is the modulus of rigidity or shear modulus of the participating rocks, A is the area of rupture of the surface of the fault at the origin of the earthquake and d is the average dislocation representing the offset in displacement between opposing fault planes. The unit of measurement for M_o is Newton meters. Seismic magnitude scales are used to quantify and categorise earthquakes based on their seismic moment. They are the actual measures of earthquake magnitude. Examples of these are moment magnitude scale (M_w), Richter magnitude scale (M_L) and modified Richter magnitude scale. On a moment magnitude scale this is defined by Hanks and Kanamori (1979) as

$$M_w = \frac{\log M_0 - 9.1}{1.5} \quad [4]$$

Albeit more tasking, moment magnitudes can also be calculated in terms of the energy released. An expression for this is derived for earthquake (Hanks and Kanamori, 1979; Borman and Giacomo, 2011):

$$M_e = \frac{\log E_s - 4.8}{1.5} \quad [5]$$

Where, M_e is the energy magnitude and E_s is the radiated seismic energy. Equation 5 is applicable in calculating the magnitude of an acoustic emission event based on the energy released (Ji and Di, 2013; Hazard and Young, 2000).

2.2 **Source plots**

Seismic moment tensors can be applied in defining seismic point sources. They describe the equivalent forces of general seismic point sources which can be related to physical events such as fault displacement (Jost and Herrmann, 1989). They are grounded on the principle of generalised force couples and are applicable to all manner of seismic sources including earthquakes, implosions, explosions, fluid-induced ruptures, landslides and rock falls. The moment tensor indicates the strength of the seismic source. It is a symmetric $3x3$ matric composed of six independent components. The moment tensor consists of a system of force couples. The diagonal elements denote linear vector dipoles, while the non-diagonal elements denote force couples with moment. The equivalent forces can be obtained if the eigenvalues and eigenvectors of the moment tensor are known. A principal axis transformation of the moment tensor can be determined by diagonalising it such that the eigenvalues represent the diagonal component of the moment tensor with the force couples acting in the direction of the principal axes (Jost and Herrmann, 1989).

In terms of its principal coordinate system, the moment tensor can be decomposed into three main types of sources: isotropic, double couple (DC) and compensated linear vector dipole (CLVD) (Vavryčuk, 2015a). The sum of the eigenvalues determines whether there is an occurrence of a volume change and its nature, if so. Volume change is associated with the presence of the isotropic component of the moment tensor. If the sum of eigenvalues is positive, the isotropic component is caused by an explosion; whereas, a negative sum of eigenvalues indicates an isotropic component caused by an implosion (Jost and Hermann, 1989). A zero-sum of eigenvalues implies that the moment tensor is only composed of

deviatoric components. In its principal coordinate system, the deviatoric moment tensor denotes a pure double couple source if one of the three eigenvalues vanishes (i.e., equals zero). If all eigenvalues are non-zero but their sum vanishes, then the moment tensor can be decomposed into a compensated linear vector dipole (CLVD). A pure isotropic source signifies an incidence of either explosion or implosion; whereas, a double couple (DC) or a compensated linear vector dipole (CLVD) source is associated with shear mechanisms. The compensated linear vector dipole source is also correlated to fracture opening and closing (Maolod, 2016; Pettitt, 1998).

From the source mechanism it is possible to determine the causes of seismic events. That is, ascertaining whether it is caused by tensile fracturing, shear fracturing, movement of an existing fault, etc. In reality numerous events take place simultaneously, making it necessary and more meaningful to visualise them together to get a holistic perspective. Source plots are important in this regard and are useful for analysing a large population of events. The diamond τ-k plot is a common example of a source plot. It is a parametric reflection of the diagonalised moment tensor. This tensor is decomposed into two parts (Hudson *et al*., 1989): isotropic and non-isotropic (deviatoric). The former can be designated by a single scalar associated with pure dilation at the source, and the k parameter of the τ-k plot is an indication of relative dilation. k ranges from +1 to -1, signifying pure implosion and explosion respectively. The latter (non-isotropic part) is represented by the τ parameter, a measure of the constant-volume or deviatoric component. This ranges from -1 through 0 (at the origin) to +1, signifying a pure negative CLVD, a pure double couple and a pure positive CLVD respectively (Vavryčuk, 2015a; Vavryčuk, 2015b). It is noteworthy that the convention for CLVD is reversed in Hudson *et al*. (1989), where τ ranges from -1 through 0 to +1, which is, instead, denoted by a pure positive CLVD, a pure double couple and a pure negative CLVD respectively.

In a three-dimensional space, the eigenvalue can be expressed as (Vavrycuk, 2015a; Vavrycuk, 2015b)

$$m = m_1\hat{e}_1 + m_2\hat{e}_2 + m_3\hat{e}_3 \qquad [6]$$

Where $\hat{e}_1$, $\hat{e}_2$ and $\hat{e}_3$ are the eigenvectors in the direction of the three principal axes of the coordinate system. The eigenvalues should satisfy the condition given in Equation 7.

$$m_1 \geq m_2 \geq m_3 \qquad [7]$$

Considering a normalised moment tensor in Euclidean space (M_E), where

$$m_i = tr(M_E) + m_i^* \qquad [8]$$

and

$$m_1^* \geq m_2^* + m_3^* \qquad [9]$$

The τ and k parameters—plotted in the vertical and horizontal axis respectively—are bounded by the following conditions (Maolod, 2016; Pettitt, 1998)

$$k = \frac{\left(\frac{1}{3}\right) tr(M_E)}{\left(\frac{1}{3}\right) tr(M_E) - m_1^*} \qquad when\ m_2^* \geq 0 \qquad [10a]$$

$$k = \frac{\left(\frac{1}{3}\right) tr(M_E)}{\left(\frac{1}{3}\right) tr(M_E) + m_3^*} \qquad when\ m_2^* \leq 0 \qquad [10b]$$

$$T = \frac{-2m_2^*}{m_1^*} \qquad when\ m_2^* > 0 \qquad [10c]$$

$$T = 0 \qquad when\ m_2^* = 0 \qquad [10d]$$

$$T = \frac{2m_2^*}{m_3^*} \qquad when\ m_2^* < 0 \qquad [10e]$$

3 **The DEM technique and seismic modelling**

Formulations pertaining to the DEM particle assembly including more detailed descriptions about the micro properties are reported in Itasca Consulting Group (2005), Poytondy and Cundall (2004), Eshiet and Sheng (2013, 2014) and other related literature. DEM is a particle-based numerical method, where individual particles are interconnected and interact via contacts. Rock is represented as an assembly of particles bonded together at contacts. The breakage of each bond between particles is considered a microcrack, with the location of this crack being the same as the contact position. Each crack is aligned perpendicular to the line that connects the two centres of adjoining particles. The breakage of a bond, signifying the simultaneous creation of a microcrack, generates acoustic energy which is transmitted through the rock body. The released energy is associated with the built-up strain energy stored during the particle genesis procedure and application of external stresses. The strain energy stored at each particle contact (E_c) is calculated as (Hazzard and Young, 2000)

$$E_c = \frac{1}{2}\left[\frac{|F^n|^2}{k^n} + \frac{|F^s|^2}{k^s}\right] \qquad [11]$$

Where F^n is the normal- contact force, F^s is the magnitude of the total shear- contact force, k^n is the contact normal stiffness and k^s is the contact shear stiffness. When there is a tensile bond breakage, the strain energy is converted to particle kinetic energy, but not all strain energy contribute to particle motion because of losses from damping, particle friction, *etc*. The particle kinetic energy (E_k) corresponding to contact bond breakage is determined according to (Hazzard and Young, 2000) as

$$E_k = \frac{1}{2}\left(mv_x^2 + mv_y^2 + I\omega^2\right) \qquad [12]$$

Where m, v, I and ω is the particle mass, velocity, moment of inertia and angular velocity respectively. The seismic source involves the pair of contacting particles associated with the micro crack. Once there is bond breakage, the source particles move and surrounding contacts with other particles are displaced, resulting in changes in forces on the affected neighbouring contacts. It is then possible to calculate the moment tensor from force changes and contact positions by integrating around the contributing contacts. The moment tensor

(M_{ij}) represents a seismic event through a group of equivalent forces that cause the same magnitude of displacement as the physical force at the source (Hazzard and Young, 2004). This is computed based on the following (Hazzard and Young, 2004, Hazzard and Young, 2002):

$$M_{ij} = \sum_{S} \Delta F_i R_j \qquad [13]$$

Where, S is the surface enclosure of the event, ΔF is the change in contact force and R is the distance between the contact position and the centroid of the event. The centroid is the point of the broken contact or the geometric centre of the event comprising more than one broken contact.

In Hazzard (1998), fracture is assumed to propagate through the rock at half the velocity of the shear wave, and the duration of an event (t_d) is taken as double the time taken for the shear wave to propagate from the source point to the edge of the area and is expressed as

$$t_d = 2\left[\frac{r_{avg}}{C_f v_s^w}\right] \qquad [14]$$

In Equation 14, r_{avg} is the average particle radius, C_f is the combination factor and v_s^w is the shear wave velocity per time step. Hazzard's model (Hazzard, 1998) does not account for the motion of particles surrounding the source cracks in a robust manner. In this study, the contacts of nearby particles is assumed to have an effect on the seismic event. Moments are calculated for all active and contributing contacts that form an event. Two or more cracks can be clustered to make up an event and the time period of event varies but can be explicitly controlled. This allows for a more accurate magnitude of b_value to be achieved.

4 **Seismicity due to triaxial loading, fluid injection and fracturing**

This section illustrates the DEM modelling of seismicity and fracturing during triaxial loading. The numerical model is built to replicate physical laboratory experiments reported in Pettitt (1998). The synthetic sample is cube-shaped with an edge length of 0.588 m, comprised of particles with radius ranging between 7.5e-4 m and 1.27e-3 m. Particles are joined together with a cementitious material mimicked by the parallel bond model. In DEM, this type of particle assemblage built by the PFC (Particle Flow Code) program is termed the *bonded-particle model* (BPM). BPM is an ensemble of densely packed irregular-sized circular/spherical particles joined together by parallel-bonds (Potyondy and Cundall, 2004). It can, thus, be calibrated to imitate the behaviour of rock. The macro mechanical properties of both real and synthetic rock are the same and are presented in Table 1 for Springwell sandstone. This type of sandstone is a deposit of the Upper Carboniferous (Stirling, *et al*, 2013) and Permian period. They are fine to medium grained with low-medium strength and are generally homogeneous, isotropic and linearly elastic (Stirling, *et al*, 2013; Alsayed, 2002; Alsayed, 1996; Tecen, 1992).

Numerical triaxial and uniaxial compression tests were performed on the synthetic rock sample. A 2 MPa confining stress was maintained during the triaxial test, while the vertical load was gradually increased to approximately 65 MPa. For the uniaxial compression test, the vertical load was increased in a likewise manner to about 47 MPa. In the course of the triaxial compression test, acoustic emission events were monitored. In the laboratory experiment, 1175 events were recorded but only 87 were considered to be pronounced and, thence, used to calculate the b_value and to generate a *t-k* plot to identify the source type of events. Magnitudes of acoustic emissions were calculated according to Equation 13. For better resolution and visualisation, it was necessary to combine two or more incidences of

acoustic emission into a single cluster to represent an event. This was achieved by adjusting the combination factor in Equation 14 according to the following sequence: 5, 6, 10 and 15.

No data is given for sandstone bulk density; however, for the given porosity (ϕ) of 0.35, the bulk density can be determined from the particle density (ρ_p). A representative particle density for sandstone is 2650 kg/m^3 (Eshiet and Sheng, 2014). The bulk density (ρ_b) can, thus, be estimated as follows

$$\rho_b = \rho_p(1-\phi) \qquad [15]$$

$$= 1722.5\ kg/m^3$$

Table 1 Key mechanical properties of Springwell sandstone

Rock property	Experiment			
	Triaxial compression test (confined)		Uniaxial compression test (unconfined)	
	Actual rock	Synthetic rock	Actual rock	Synthetic rock
Young modulus (GPa)	14.1	11.75-13.03	12.2	11.37-13.03
Poisson ratio	0.294	0.290-0.298	0.355	0.372-0.329
Compressive strength (MPa)	64.3	55.87-59.50	46.7	47.0-49.0

A fluid injection test was also performed as a replica of the physical laboratory experiment on granite presented in Matsunaga *et al.* (1993). In this test, high pressure fluid is injected at the centre of a cubic-shaped granite sample with a side length of 0.2 m. The sample is biaxially loaded by an applied vertical and horizontal stress of 12.2 MPa and 6 MPa respectively. Fluid was injected continuously until the first sign of fractures at the edge of the sample. For the numerical model, the algorithm and governing parameters for fluid injection and flow in DEM is adopted from Eshiet and Yang (2014). The main mechanical properties of granite are given in Table 2, and the corresponding DEM micro properties for a given range of particle radius size, 0.0025 m – 0.00625 m, are given in Table 3.

Table 2 Key mechanical properties of Inada granite (Lin and Takashi, 2008; Lin, 2002)

Parameter	Value
Young modulus (GPa)	62
Poisson ratio	0.30
Uniaxial compressive strength (MPa)	200
Tensile strength (MPa)	3.99-8.74
Permeability (m2)	1.08e-16
Porosity (%)	0.75

Table 3 Micro mechanical properties for synthetic rock samples

Parameter	Value	
	Sandstone	Granite
Particle size ratio ($\boldsymbol{R_{ratio}}$)	1.66	2.5
Minimum particle radius ($\boldsymbol{R_{min}}$)	7.5e-4 m	2.5e-3 m
Particle friction coefficient ($\boldsymbol{\mu}$)	0.5	0.5
Particle stiffness ratio ($\boldsymbol{k_n/k_s}$)	2.5	2.5
Particle Young Modulus ($\boldsymbol{E_c}$)	15 GPa	62 GPa
Tensile strength of parallel bond ($\boldsymbol{\bar{\sigma}_c}$)	40 MPa	330 MPa
Shear strength of parallel bond ($\boldsymbol{\bar{\tau}_c}$)	40 MPa	270 MPa

5 Results and discussion

A visual representation of the acoustic emissions for the real and synthetic sandstone sample is illustrated in Figure 1. The locations of acoustic emissions are plotted according to their hypocentres. The hypocentre is the point of rupture, or put more precisely, the central point of bond breakage between particles. It is possible to combine incidences of acoustic emission such that several sources are merged into one event. This requires the introduction of a combination factor which is one of controlling parameters that guide the grouping of individual acoustic emissions into clusters. One of the major problems with the use of acoustic emissions to image the failure process of materials is the difficulty in tracking hypocentres. Certain advances has been made in this regard for real life earthquakes through techniques such as the *Geiger location*, the *master event relative relocation* and the *double difference relocation* method (Jones, *et al*., 2008).

The Hazzard's DEM model (Hazzard, 1998) applies a constant combination factor, which causes large variances with physical experimental observation of microseismic events. In Pettitt's physical experiment (Pettitt, 1998), 1175 acoustic emission events were identified; however, in Hazzard's simulation of the same experiment only 995 acoustic emission events were marked. A variable combination factor of the source is adopted for the model in this study, which means there is no fixed criterion as to what constitutes an event with respect to the nature, number and combination of singular origins of acoustic emission. Through this approach, 1220 acoustic emission events are recorded, providing a much improved reproduction of the laboratory signals (Figure 1). It is then possible –as facilitated by an inconstant combination factor–to calibrate the procedure for registering events such that the resolution captured through real life instrumentations, e.g., geophones can be replicated. In the DEM fluid injection test on synthetic granite, 550 acoustic emission events were registered. The population of events, though slightly higher, is near to the 496 acoustic emission hypocentres recorded in Matsunaga *et al.* (1993) for a similar experimental set-up.

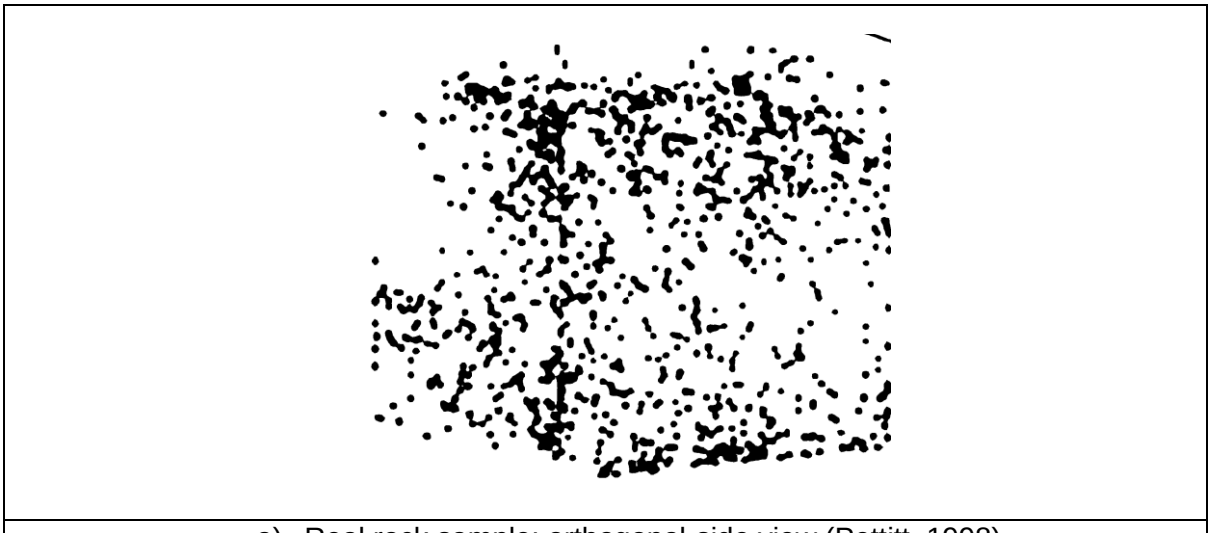

a) Real rock sample: orthogonal-side view (Pettitt, 1998)

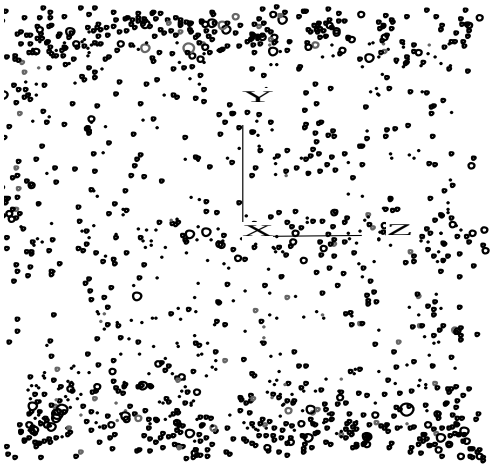

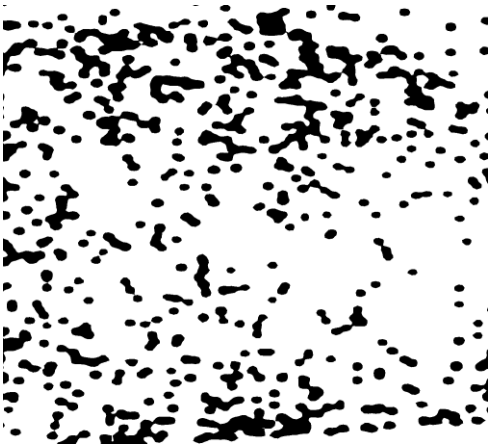

b) Synthetic rock sample

c) Real rock sample: right side view (Pettitt, 1998)

Figure 1 Distribution of acoustic emission events after compression test

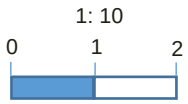

5.1 **The seismic *b-value* and source plot**

The seismic b-value (b) is a crucial part of Equation 1-2 and defines the distribution of magnitude of acoustic emission events. The distribution of the magnitudes of natural earthquake normally follows a power-law trend defined by the relationship between the number of events and the size of the seismic event (Hazzard and Young, 2004). Mathematically, this is described by the *Gutenberg-Richter* law given by Equation 2. The b_value is derived from the curve ascribed to the *Gutenberg-Richter* type relationship and denotes the slope of the near-vertical section of the line. For natural earthquakes, a b_value of approximately 1 is generally expected. It is, therefore, reasonable to envisage that the b_value for acoustic emission sequence of events which follow the same *Gutenberg-Richter* type law should also be close to unity. Instead, higher b_values are commonly observed, as severally reported for various laboratory-scale experiments on different types of rocks. From laboratory studies, a b_value of up to 2.4 has been derived for sandstone and granite (Hazzard and Young, 2004; Pettitt, 1998; Lockner *et al*., 1991). Higher b_values are typically noticed in small-scale studies of acoustic emissions. In Pettitt's laboratory test (Pettitt, 1998), a b_value of 2.36 was obtained, but a much lower value (b_value = 1.66) was determined by Hazzard (Hazzard, 1998) (Figure 2). A closer match to the laboratory tests results in Pettitt (1998) is attainable (b_value = 2.28) by incorporating a procedure whereby the combination factor is periodically and sequentially altered in ascension.

Nonetheless, for the DEM fluid injection test, the computed b_value is 0.92, illustrated by the light shaded/green section of the curve in Figure 3. This value is closer to unity and the range of b_values normally encountered in field scale natural environments. The proximity of the b_value from the DEM fluid injection test to unity can be attributed to the larger range of particle sizes used in building the granite sample in relation to sandstone. For the synthetic samples, b_value is dependent on particle size, increasing when the particles are smaller in size.

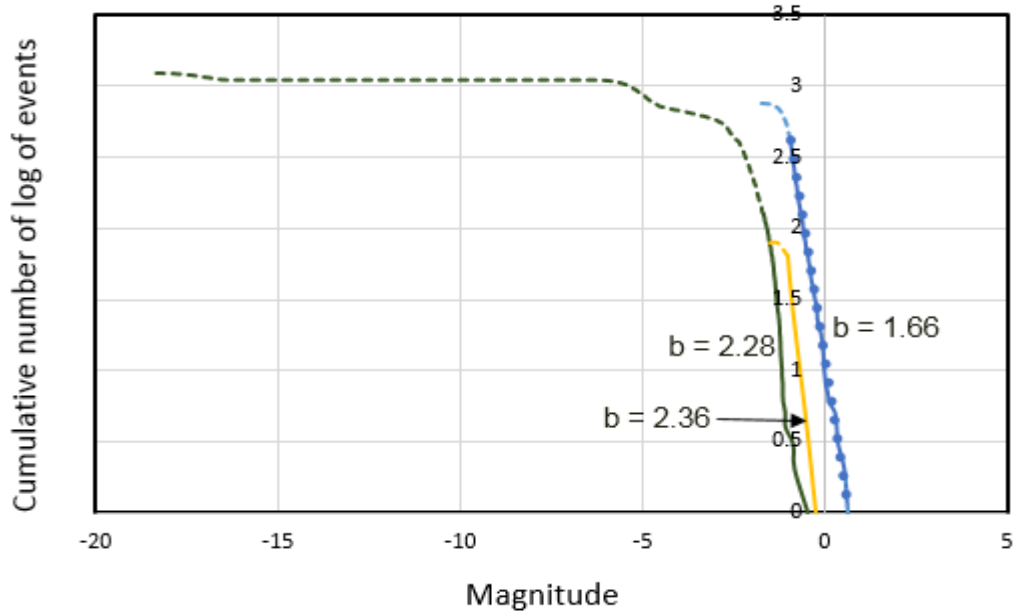

Figure 2 Frequency-magnitude distribution for acoustic emission in DEM and laboratory experiment rock sample (blue: fixed C_f, yellow: data from experiment, and green: changeable C_f)

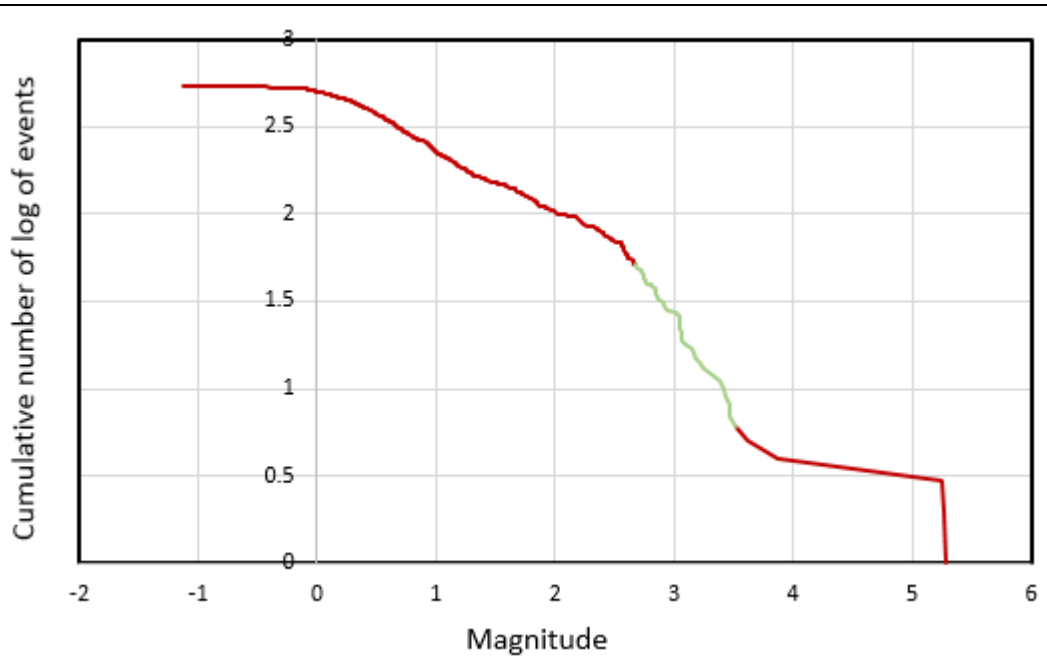

Figure 3 Frequency-magnitude distribution for acoustic emission during fluid injection in DEM model

Source plots in the form of τ-k plots for the compression laboratory experiment, and the corresponding DEM imitations of both compression and fluid injection are presented in Figure 4-5. The τ-k plot space delineates the boundaries of the limits of the isotropic (dilatational) and deviatoric (constant-volume) component of the seismic source mechanisms. As described in Section 2, the *k*-axis shows the scale of dilatational

mechanisms ranging from pure implosion to pure explosion. The τ-axis, on the other hand, defines the bounds of deviatoric and constant volume mechanisms. At the centre, there is zero dilation and *CLVD* but a full double-couple source mechanism, which signifies shear cracking. Positive values of *k* and *CLVD* (i.e., $\tau = +ve$) are associated with tensile mechanisms. Conversely, negative values of *k* and *CLVD* (i.e., $\tau = -ve$) indicate compressive mechanisms; however, there is a tendency for tensile cracks to occur as the linear vector dipole approaches $\tau = \pm 1$ (Vavryčuk, 2015a). From Figure 4-5, it is shown that whilst there are no extreme cases of implosion and explosion sources, the set of seismic sources comprises a complex combination of tensile, compressive and shear mechanisms. The distribution of seismic source mechanisms exhibited in the proposed DEM τ-k plot qualitatively matches results from the laboratory experiment (Figure 4). Obviously, there are fewer data points included in the laboratory test plot; only 87 out of 1175 acoustic emission events were considered clear enough to be used. Simulated results from the fluid injection tests show a larger proportion of tensile-induced source mechanisms as indicated by the large clustering of events near the linear vector dipoles given by $k = 1, \tau = \pm 1$, and most importantly, away from the plot origin where DC = 1 (Figure 5).

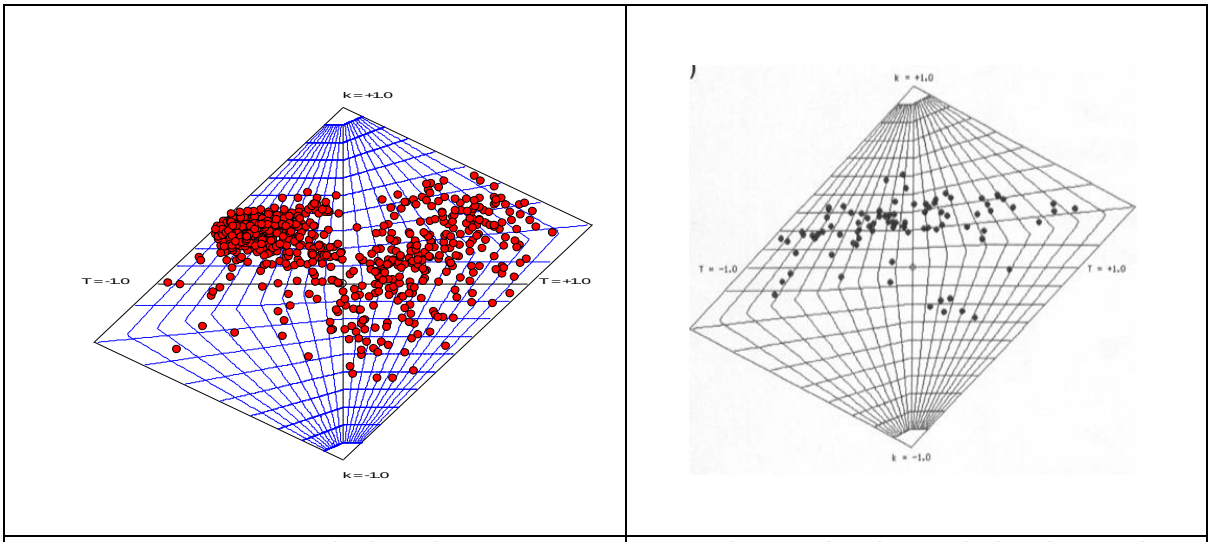

a. Synthetic rock

b. Real rock sample (Pettitt, 1998)

Figure 4 *t-k* plot for DEM and laboratory test sample

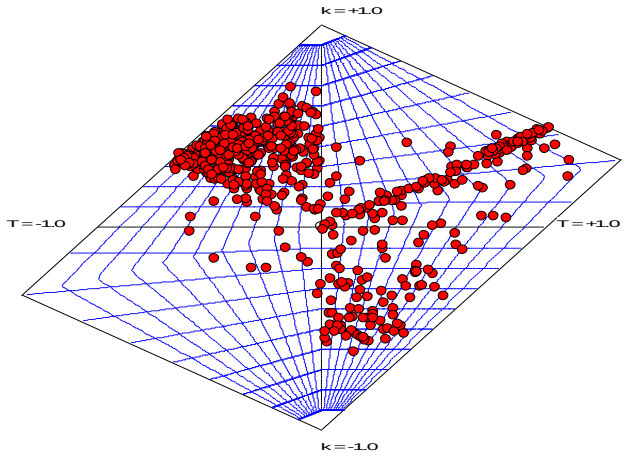

Figure 5 *t-k* plot generated during fluid injection by DEM

5.2 **Fracture aperture**

The average opening mode displacement or crack aperture can be determined from its correlative relationship with crack length. Building on previous derivations by Oslo (2003), Klimczak *et al*. (2010) established a correlation between the average gap separating opposing walls of an open mode fracture and its corresponding length. At the micro scale this relationship, expressed in Equation 15, can be applied to individual open mode (tensile) cracks.

$$A_{ap} = \frac{\pi\alpha}{4}\sqrt{L} \qquad [16a]$$

$$\alpha = \frac{\sqrt{8}}{\sqrt{\pi}}\left[\frac{K_{Ic}(1-\nu)^2}{E}\right] \qquad [16b]$$

The parameter α is the average proportionality constant, L is the crack length, K_{Ic} is the fracture toughness, ν is the Poisson ratio and E is the elastic modulus. The estimated crack aperture for the compression and fluid injection test is $\leq$ 1e-5 m and $\leq$ 1e-4 m respectively (Figure 6-7). The computed crack apertures for the fluid injection test is within the same bounds as those reported by Frash *et al* (2014) for similar experiments.

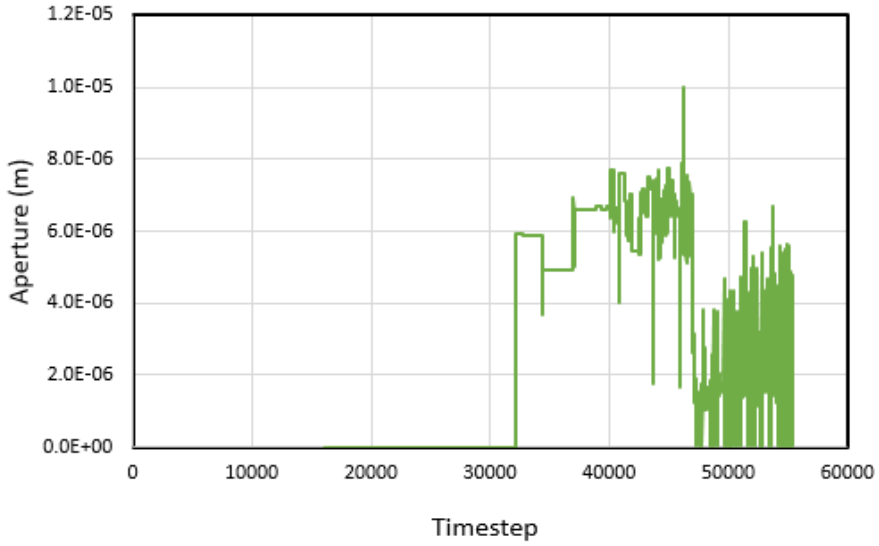

Figure 6 Crack apertures during simulated compressive loading

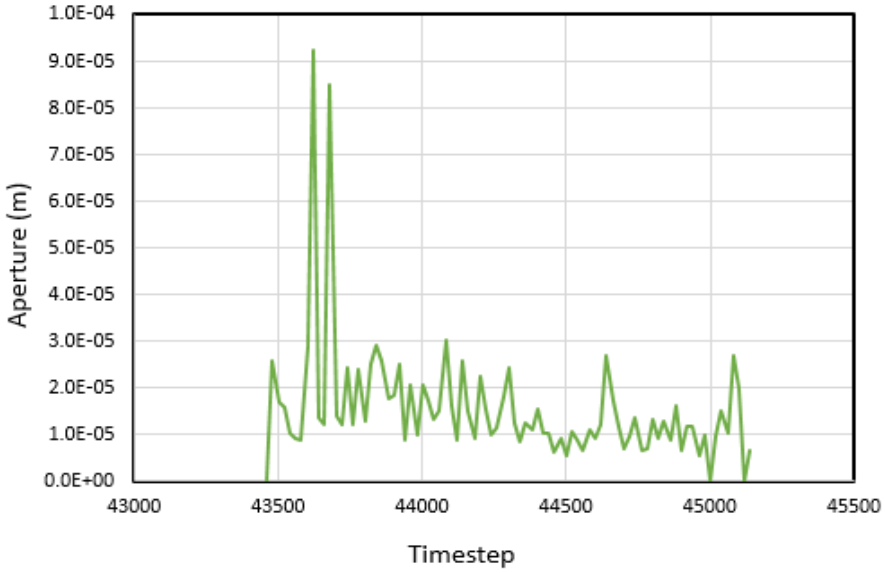

Figure 7 Crack apertures created during fluid injection

6 **Conclusion**

The formulation of numerical simulations based on the discrete element method to reproduce and/or predict seismicity is ongoing and efforts are still being made to advance the capability of this modelling technique. Hazzard (Hazzard, 1998) introduced a set of concepts and algorithms to model the occurrence of acoustic emissions and microseimicity events specifically generated due to the creation of cracks in rocks. The procedure has been amended to overcome some of the difficulties to accurately simulate induced seismicity, especially those caused by externally applied stress and fluid flow within solid materials. A crucial aspect of this modification is the incorporation of a changeable combination factor which permits the application of a flexible set of criteria for the selection of participating neighbouring particles and contacts. This has enabled improved imaging of rock failure and

the tracking of hypocentres of seismic events, reflected via enhancements in four main areas: accurate spatial and temporal tracing of acoustic emissions, b_values that are realistic and representative of actual occurrence in both small-scale physical laboratory experiments and real life (field-scale) scenarios, resolution and visualisation of source mechanisms, and the creation of similar sizes of cracks aperture with those observed in physical experiments. Further work is contemplated to develop a systematic procedure that will allow the generation of b_values that are close to those applicable in field-scale natural environments rather than physical laboratory experiments, which produce results that could be limited in some aspects due to scaling effects.

References

Aker, E., Kuhn, D., Vavrycuk, V., Soldal, M. and Oye, V. (2014) Experimental investigation of acoustic emissions and their moment tensors in rock during failure. International Journal of Rock Mechanics & Mining Sciences. 70. pp. 286–295.

Aki, K. (1967) Scaling law of seismic spectrum. Journal of Geophysical Research. 72 (4). pp. 1217-1231.

Aki, K. (1966) Generation and propagation of G waves from the Niigata earthquake of June 16, 1964. Part 2. Estimation of earthquake moment, released energy, and stress-strain drop from the G wave spectrum. Bull. Earthquake Res. Inst., Tokyo Univ. 44. pp. 73-88.

Al-Busaidi, A., Hazzard, J., and Young, R. (2005) Distinct element modeling of hydraulically fractured Lac du Bonnet granite: Journal of geophysical research. 110. B06302.

Alsayed, M. I. (1996) Rock behaviour under multiaxial compression. PhD Thesis. University of Newcastle upon Tyne

Alsayed, M. I. (2002) Utilising the Hoek triaxial cell for multiaxial testing of hollow rock cylinders. Int. J. Rock Mech. Min. Sci. 39. pp. 355–66.

Bormann, P. and Di Giacomo, D. (2011) The moment magnitude, M_w, and the energy magnitude M_e: common roots and differences. J Seismol. 15. pp. 411–427.

Cheon, D.-S., Park, E.-S., Jung, Y.-B., Park, C. and Synn, J.-H. (2008) Tunnel and Underground Space. 18 (1). pp. 1-9.

Eshiet, K. I., Sheng, Y. and Ye, J. (2013) Microscopic Modelling of the Hydraulic Fracturing Process. Environmental Earth Sciences. 68 (4). pp. 1169-1186.

Eshiet, K. I. and Sheng, Y. (2014) Investigation of Geomechanical Responses of Reservoirs Induced by Carbon Dioxide Storage. Environmental Earth Sciences. 71. pp. 3999-4020.

Filipussi, D. A., Guzman, C. A., Xargay, H. D., Hucailuk, C. and Torres, D. N. (2015) Study of acoustic emission in a compression test of andesite rock. Procedia Materials Science. 9. pp. 292-297.

Foulger, G. R., Wilson, M. P., Gluyas, J. G., Julian, B. R. and Davies, R. J. (2018) Global review of human-induced earthquakes. Earth Science Reviews. 178. pp. 438-514.

Frash, L. P., Hood, J., and Gutierrez, M. (2014) Laboratory measurement of critical state hydraulic fracture geometry. 48th US Rock Mechanics/Geomechanics Symposium, MN, USA, 1-4 June, Minneapolis.

Graham C. C., Stanchits, S., Main, I. G., Dresen, G. (2010) Comparison of polarity and moment tensor inversion methods for source analysis of acoustic emission data. International Journal of Rock Mechanics & Mining Sciences. 47. pp. 161–9.

Gutenberg, B. and Richter, C. F. (1956) Earthquake magnitude, intensity, energy, and acceleration (Second Paper): Bull. Seism. Soc.

Hanks, T. C. and Kanamori, H. (1979) A Moment magnitude scale. Journal of Geophysical Research. 84 (B5). pp. 2348–50.

Hazzard, J. F. and Young, R. P. (2004) Dynamic modelling of induced seismicity. International journal of rock mechanics and mining sciences. 41 (8). pp. 1365-1376.

Hazzard, J. F. and Young, R. P. (2002) Moment tensors and micromechanical models. Tectonophysics. 356. pp. 181–197.

Hazzard, J. F. and Young, R. P. (2000) Simulating acoustic emissions in bonded particle models of rock. International Journal of Rock Mechanics and Mining Sciences. 37 (5). pp. 867–72.

Hazzard, J. F. (1998) Numerical modelling of acoustic emissions and dynamic rock behaviour. PhD Thesis. Keel University

Hu, X. and Jia, X. (2016) A dynamic lattice method for elastic seismic modeling in anisotropic media. Geophysics. 81 (3). pp. T131–T143.

Hudson, J. A.; Pearce, R. G. and Rogers, R. M. (1989) Source Type Plot for Inversion of the Moment Tensor. Journal pf Geophysical Research. 94, B1. pp. 765-774.

Itasca Consulting Group, (2005) Particle Flow Code PFC 3D user's manuals, version 4. Minneapolis, Minnesota

Ji, S. and Di, S. (2013) Discrete element modeling of acoustic emission in rock fracture. Theoretical & Applied Mechanics Letters. 3, 021009.

Jones, G. A., Nipprress, S. E. J., Rietbrock, A. and Reyes-Montes, J. M. (2008) Accurate location of synthetic acoustic emissions and location sensitivity to relocation methods, velocity perturbations, and seismic anisotropy. Pure and Applied Geophysics. 165. pp. 235–254.

Jost, M. L. and Hermann, R. B. (1989) A Student's Guide to and Review of Moment Tensors. Seismological Research Letters. 60 (2). pp. 37-57.

Klimczak, C., Schultz, R. A., Parashar, R. and Reeves, D. M. (2010) Cubic law with aperture-length correlation: implications for network scale fluid flow. Hydrogeology Journal 18 (4): 851-862.

Lei, X., Funatsu, T., Ma, S. and Liu, L. (2016) A laboratory acoustic emission experiment and numerical simulation of rock fracture driven by a high-pressure fluid source. Journal of Rock Mechanics and Geotechnical Engineering 8, 27-34.

Lei, X. and Ma, S. (2014) Laboratory acoustic emission study for earthquake generation process. Earthquake Science (2014) 27 (6): 627–646.

Lin, W. and Takashi, M. (2008) Anisotropy of strength and deformation of Inada granite under uniaxial tension. Chinese journal of rock mechanics and engineering. 22. 12.

Lin, W. (2002) Permanent strain of thermal expansion and thermally induced microcracking in Inada granite. Journal of geophysical research. 107. B10.

Lisjak, A. and Grasselli, G. (2014) A review of discrete modeling techniques for fracturing processes in discontinuous rock masses. Journal of Rock Mechanics and Geotechnical Engineering. 6. pp. 301-314.

Lisjak, A., Liu, Q., Zhao, Q., Mahabadi, O. K. and Grasselli, G. (2013) Numerical simulation of acoustic emission in brittle rocks by two-dimensional finite-discrete element analysis. Geophysical Journal International. 195. pp. 423-443.

Lockner, D. A., Byerlee, J. D., Kuksenko, V., Ponomarev, A. and Sidorin, A. (1991) Quasi-static fault growth and shear fracture energy in granite. Nature. 350. pp. 39-42.

Maghsoudi, S., Baro, J., Kent, A., Eaton, D. and Davidson, J. (2018) Interevent triggering in microseismicity induced by hydraulic fracturing. Bulletin of the Seismological Society of America. 108 (3A). pp. 1133–1146.

Maolod, R. R. (2016) The Use of Microseismic Monitoring as a Guide for Gas Production. PhD Thesis. University of Leeds

Matsunaga, I., Kobayashi, H., Sasaki, S. and Ishida, T. I. (1993) Studying hydraulic fracturing mechanism by laboratory experiments with Acoustic emission monitoring. Int. J. Rock Mech. Min. Sci. & Geomech. Abstr. 30 (7). pp. 909-912.

Michlmayr G., Denis, C. and Dani, O. (2012) Sources and characteristics of acoustic emissions from mechanically stressed geologic granular media—a review. Earth Sci. Rev. 112. pp. 97–114.

Mohammadipour, A. and Willam, K. (2015) Lattice approach in continuum and fracture mechanics. Journal of Applied Mechanics. 83. 071003.

O'Brien, G. S. and Bean, C. J. (2011) An irregular lattice method for elastic wave propagation. Geophys. J. Int. 187. pp. 1699–1707.

Olson, J. E. (2003) Sublinear scaling of fracture aperture versus length: an exception or the rule? Journal of geophysical research. 108. B9.

Pettitt, W. S. and King, M. S. (2007) Laboratory measurements of acoustic emissions and wave velocities associated with the formation of fractures in sandstones. Lonergan, L., Jolly, R. J. H., Rawnsley, K. and Sanderson, D. J. (eds) Fractured Reservoirs. Geological Society, London, Special Publications. 270. pp. 93-99.

Pettitt, W. S. (1998) Acoustic emission source studies of microcracking in rock. PhD Thesis. Keel University

Potyondy, D. O. and Cundall, P. A. (2004) A bonded-particle model for rock. International journal of rock mechanics and mining sciences. 41 (8). pp. 1329-1364.

Rothert, E. and Shapiro, S. A. (2003). Microseismic monitoring of borehole fluid injections: Data modeling and inversion for hydraulic properties of rocks. Geophysics. 68 (2). pp. 685-689.

Scholz, C. H. (1968) The frequency-magnitude relation of microfracturing in rock and its relation to earthquakes. Bulletin of the Seismological Society of America. 58 (1). pp. 399-415.

Stirling, R., Simpson, D. and Davie, C. (2013) The application of digital image correlation to Brazilian testing of sandstone. International Journal of Rock Mechanics and Mining Sciences. 60. pp. 1-11.

Tang, C. (1997) Numerical simulation of progressive rock failure and associated seismicity. Int. J. Rock Mech. Min. Sci. 34 (2). pp. 249–261.

Tang, C. A. and Kaiser, P. K. (1998) Numerical simulation of cumulative damage and seismic energy release during brittle rock failure—part I: fundamentals. Int. J. Rock Mech. Min. Sci. 35 (2). pp. 113–121.

Tecen, O. (1992) High pressure water jet assisted drag tool cutting of rock materials. PhD Thesis. University of Newcastle upon Tyne

Vavryčuk, V. (2015a) Moment Tensors: Decomposition and Visualization. Encyclopedia of Earthquake Engineering. DOI 10.1007/978-3-642-36197-5_288-1.

Vavryčuk, V. (2015b) Moment tensor decompositions revisited. J Seismol. 19. pp. 231–252.

Wangen, M. (2018) A 2D Model of hydraulic fracturing, damage and microseismicity. Pure and applied geophysics. 175. pp. 813–828.

Wang, Y. C. (2008) Discrete element simulation of hydraulic fracturing and induced seismicity in engineered geothermal systems. Australian Geothermal Energy Conference

Yoon, J. S., Zang, A., Stephansson, O., Hofmann, H. and Zimmermann, G. (2017) Discrete element modelling of hydraulic fracture propagation and dynamic interaction with natural fractures in hard rock. Procedia Engineering. 191. pp. 1023 – 1031.

Yoon, J. S., Zimmermann, G., Zang, A. and Stephansson, O. (2015) Discrete element modeling of fluid injection–induced seismicity and activation of nearby fault. Can. Geotech. J. 52. pp. 1457–1465.

Young, R. P. and Baker C. (2001) Microseismic investigation of rock fracture and its application in rock and petroleum engineering. International Society of Rock Mechanics News Journal. 7. pp. 19–27.

Young, R. P., Hazzard, J. F. and Pettitt, W. S. (2000) Seismic and micromechanical studies of rock fracture. Geophysical Research Letters. 27. pp. 1767-1770.

Young, R. P. and Pettitt, W. S. (2000) Investigating the stability of engineered structures using acoustic validation of numerical models, Labuz, J. F., Glaser, S. D. and Dawson, E. (eds). Geotechnical Special Publications, 102. ASCE, USA, 1-15.

Zang, A., Yoon, J. S., Stephansson, O. and Heidbach, O. (2013) Fatigue hydraulic fracturing by cyclic reservoir treatment enhances permeability and reduces induced seismicity: Geophysical journal international. 195 (2). pp. 1282-1287.

Zhao, Q., Lisjak, A., Mahabadi, O., Liu, Q. and Grasselli, G. (2014) Numerical simulation of hydraulic fracturing and associated microseismicity using finite-discrete element method. Journal of Rock Mechanics and Geotechnical Engineering. 6. pp. 574-581.

Zhu, W., Zhao, X., Kang, Y., Wei, C. and Tian, J. (2010) Numerical simulation on the acoustic emission activities of concrete, Mater. Struct. 43 (5). pp. 633-650.